Appl. Phys. A (2015) 121:625–634
DOI 10.1007/s00339-015-9447-y

Applied Physics A
Materials Science & Processing

AC conductivity and structural properties of Mg-doped ZnO ceramic

Zayani Jaafar Othman[1] · Olfa Hafef[1] · Adel Matoussi[1] · Francesca Rossi[2] · Giancarlo Salviati[2]

Received: 30 January 2015 / Accepted: 18 August 2015 / Published online: 28 August 2015
© Springer-Verlag Berlin Heidelberg 2015

Abstract Undoped ZnO and $Zn_{1-x}Mg_xO$ ceramic pellets were synthesized by the standard sintering method at the temperature of 1200 °C. The influence of Mg doping on the morphological, structural and electrical properties was studied. The scanning electron microscopy images revealed rough surface textured by grain boundaries and compacted grains having different shapes and sizes. Indeed, the X-ray diffraction reveals the alloying of hexagonal ZnMgO phase and the segregation of cubic MgO phase. The crystallite size, strain and stress were studied using Williamson–Hall (W–H) method. The results of mean particle size of $Zn_{1-x}Mg_xO$ composites showed an inter-correlation with W–H analysis and Sherrer method. The electrical conductivity of the films was measured from 173 to 373 K in the frequency range of 0.1 Hz–1 MHz to identify the dominant conductivity mechanism. The DC conductivity is thermally activated by electron traps having activation energy of about 0.09 to 0.8 eV. The mechanisms of AC conductivity are controlled by the correlated barrier hopping model for the ZnO sample and the small polaron tunneling (SPT) model for $Zn_{0.64}Mg_{0.36}O$ and $Zn_{0.60}Mg_{0.40}O$ composites.

✉ Zayani Jaafar Othman
jaafar.zayani@yahoo.fr

1 Laboratory of Composite Ceramic and Polymer Materials, Scientific Faculty of Sfax, 4000 Sfax, Tunisia

2 Institute of Materials for Electronics and Magnetism (IMEM), Parma University, 43124 Parma, Italy

1 Introduction

The interest in Zinc oxide (ZnO) has recently grown thanks to its potential use in numerous technological applications such as transparent conducting electrodes, display materials, light-emitting diodes (LED), gas sensors, solar cells, laser systems varistors [1–3]. Zinc oxide is a well-known wide-band-gap semiconductor (Eg = 3.37 eV at 300 K) with a large exciton binding energy (60 meV), high dielectric constants and low dielectric losses [4]. Hall mobility in ZnO single crystal is in the range of 5–30 $cm^2\ V^{-1}\ s^{-1}$ [5]. Intrinsically, ZnO is an n-type semiconductor whose electrical conductivity is due to the excess of zinc interstitial position [6]. This can be modified thoroughly by appropriate substitution dopants such as Fe, Al and Sn [7–9]. Besides, ZnO doped with (Cr, Mn, Fe) has attracted much attention due to the strong correlation between the structural, optical and magnetic properties [10]. In our case, we have used magnesium oxide as the Mg doping element to enhance the optical, morphological and electrical conductivity of ZnO material. In fact, Mg^{2+} has an ionic radius of 0.057 nm, which is very close to the ionic radius of Zn^{2+} (0.060 nm). Therefore, the replacement of Zn by Mg does not give rise to significant changes in lattice constants, but can significantly influence the electrical conduction in ZnO. Kılınç et al. [11] have investigated the effect of Mg on the structure and electrical properties of ZnO thin films. With the increase in Mg doping rate ($x = 0$–0.2), the DC conductivity at room temperature gradually decreased from 3.36×10^{-6} to 7.85×10^{-9} S cm^{-1}. Moreover, $Zn_{1-x}Mg_xO$ films could be obtained by simple and low-priced synthetic methods such as spray pyrolysis, sintering, pulsed laser deposition, sol–gel process and aerosol-assisted chemical vapor deposition [12–14, 17, 18]. The optical and electronic properties of those composite films were found to depend sensibly on the Mg doping concentration and the

growth conditions [11–16]. Zhao et al. [14] have obtained $Zn_{1-x}Mg_xO$ alloy films with hexagonal structure by varying the Mg composition between 0 and 36 %. The grain size and the surface roughness were reduced, while the band gap was increased in the range of 3.34 and 3.96 eV. Othman et al. [16] have found that the optical band gap increases from 3.287 to 3.827 eV and the carrier concentration augments from 1.6×10^{16} to 5.2×10^{20} cm^{-3} in ZnO and $Zn_{0.6}Mg_{0.4}O$ samples, respectively. The same result was found by the group of Shukla et al. [18], on thin films of $Mg_xZn_{1-x}O$ growth by aerosol-assisted chemical vapor deposition (AACVD) technique. Recent works [18] show that with the increase in Mg content, transparency as well as energy band gap of the $Mg_xZn_{1-x}O$ thin films increases.

The present paper sheds the light on the effect of MgO doping content on the morphological and the electrical properties of ZnO material.

2 Experimental procedure

ZnMgO pellets were synthesized by the conventional sintering technique in atmospheric heated furnace at 1200 °C. Pure powders (99.99 %) of zinc oxide and magnesium oxide (MgO) were used. The weight content (x %) of MgO was varied from 0 to 40 % and added to ZnO powder. The mixed powders were first milled in an agate and heated in air at annealing temperature of 300 °C for 3 h, to evaporate the water and remove the organic residuals. The obtained powders were then pressed into pellet disks (of about 1 mm thickness and 8 mm diameter) and sintered at 1200 °C for 24 h. Finally, these pellets were rapidly quenched to room temperature in air in order to freeze the structure. The surface morphology was characterized by scanning electron microscopy (SEM). The dielectric and electrical properties were characterized by means of Novocontrol system for broadband dielectric spectroscopy (BDS). These measurements were taken in wide frequency ranges (0.1–10^6 Hz) and temperatures (173–373 K). A flow of nitrogen was used for temperature adjustment at the pellet which was inserted between two parallel-plate electrodes ("sandwich geometry"). Likewise, a sinusoidal voltage U_0 with a fixed frequency was applied, creating an alternating electrical field which was measured perpendicularly to the disk. So, the voltage U_0 causes a current I_0 at the same frequency. This induced polarization in the pellet, which oscillated at the similar frequency but with a phase angle shift δ, was measured by comparing the applied voltage to the measured current. And the measurements of capacitance and conductance were used to calculate the real ε' and the imaginary ε'' parts of the complex permittivity.

3 Results and discussion

3.1 Morphological properties

Figure 1a–c shows the SEM images for ZnO and $Zn_{1-x}Mg_xO$ pellets. The surface morphology of all samples consists of disoriented grains and nanotubes having many shapes and sizes. The texture seems to be strongly dependent on the MgO doping concentration. In fact, the particle sizes of undoped ZnO are in the range of 100 to 500 nm (Fig. 1a), but for $Zn_{0.64}Mg_{0.36}O$ and $Zn_{0.60}Mg_{0.40}O$ pellets, its average values are between 60–300 nm, 40–200 nm, respectively. This shows that the density of the crystallites decreases, suggesting that the coalescence of the small grains is enhanced for the doped ZnO films, which reveals that the flatness of doped ZnO can improve with Mg doping as reported by Park [15]. Figure 1a–c also shows the presence of grain boundaries that are probably due to the sintering process as well as the segregation of cubic MgO and hexagonal ZnO grains. In the present case, it was found that the substitution of Zn by Mg and the existence of intrinsic defects in ZnO such as zinc interstitial and oxygen vacancies led to the increase in the carrier concentration from 1.6×10^{16} to 5.2×10^{20} cm^{-3} for undoped ZnO and $Zn_{0.60}Mg_{0.40}O$, respectively [16].

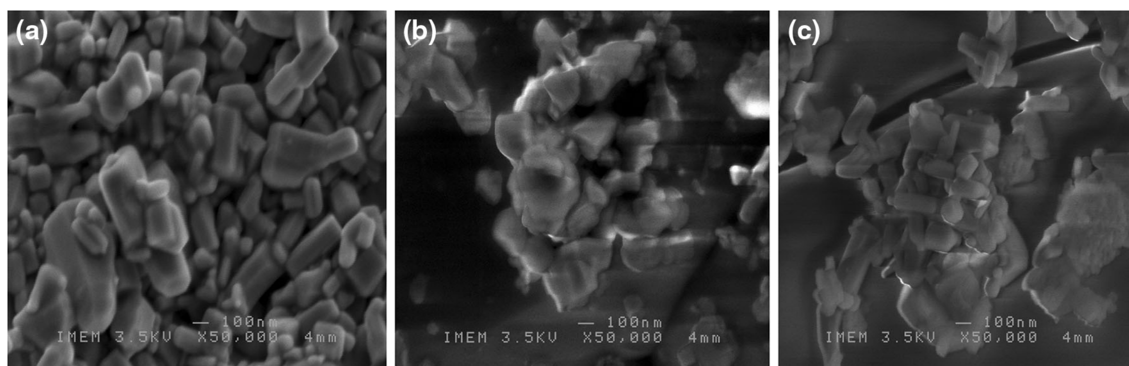

Fig. 1 SEM images obtained for pure ZnO (**a**), $Zn_{0.64}Mg_{0.36}O$ (**b**) and $Zn_{0.60}Mg_{0.40}O$ (**c**)

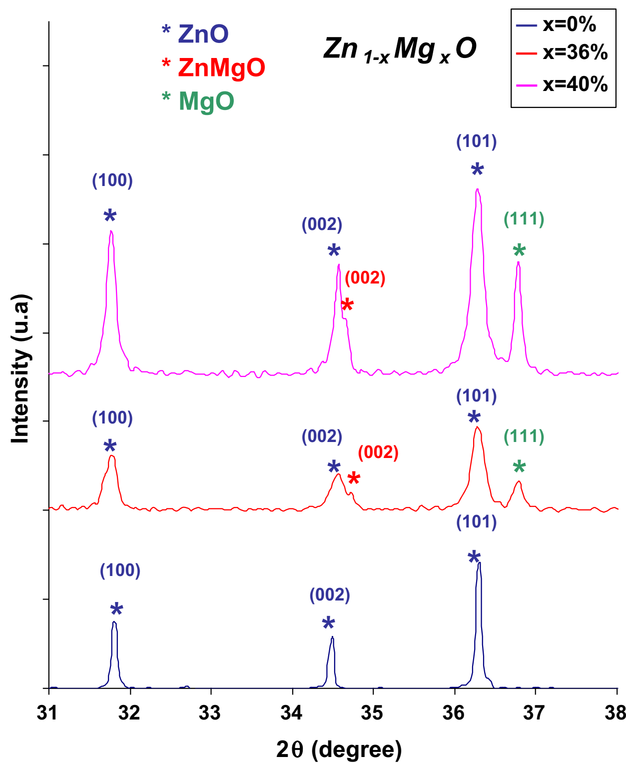

Fig. 2 XRD patterns of $Zn_{1-x}Mg_xO$ composites

3.2 Structural properties

3.2.1 XRD analysis

Figure 2 shows the XRD patterns of doped ZnO samples with different MgO contents ($x = 0$ %, $x = 36$ % and $x = 40$ %). All the samples exhibit a polycrystalline hexagonal structure. For the undoped ZnO sample, three prominent diffraction peaks were noted at $2\theta = 31.81°$, 34.47° and 36.31°, which can be attributed to the (100), (002) and (101) plane reflections of hexagonal wurtzite ZnO (JCPDS card No. 36-1451), respectively, and unit cell parameters $a = 0.3249$ nm and $c = 0.5206$ nm. It can be seen that the ZnO growth appears to be randomly oriented along the (101) and (002) planes. This reveals that the hexagonal structure of all doped ZnO samples has not been affected by the MgO doping. However, secondary phases are formed at higher concentrations. With doping content up to $x = 36$ %, a diffraction peak can be seen at 36.7°, corresponding to (111) plane of cubic MgO phase according to the standard JCPDS data card No. 78-0430. This result indicates a considerable segregation of the MgO phase in the ZnO wurtzite structure. Recently, Othman et al. [16] have shown that the limit solubility of MgO in the ZnO host is found to be $x = 10$ %. In addition, another diffraction peak appears at $2\theta = 34.68°$, which is identified at the (002) direction of hexagonal ZnMgO alloy structure [19–22]. Zheng et al. [21] showed the appearance of this diffraction peak around $2\theta = 34.7°$ in a single-crystalline wurtzite structure of $Zn_{0.51}Mg_{0.49}O$ films.

3.2.2 Crystalline size and strain

3.2.2.1 Scherrer method Crystallite size and lattice strain due to dislocation can be calculated from peak broadening using XRD [23]. X-ray line broadening method was used to determine the particle size of the $Zn_{1-x}Mg_xO$ composites using Scherrer equation. $D = (k\lambda/\beta_D \cos\theta)$, where D is the particle size in nanometers, λ is the wavelength of the radiation (0.154056 nm for CuKα radiation), k is a constant equal to 0.94, β_D is the peak width at half-maximum intensity and θ is the peak position. Both instrument- and sample-dependent effects are combination of the Bragg peak breadth. To remove these aberrations, it is needed to assemble a diffraction pattern from the line broadening of a standard material such as silicon to determine the instrumental broadening. The instrument-corrected broadening [24] β_D corresponding to the diffraction peak of $Zn_{1-x}Mg_xO$ composites was estimated using the relation:

$$\beta_D^2 = [\beta^2_{\text{measures}} - \beta^2_{\text{instrumental}}] \tag{1}$$

$$D = \frac{k\lambda}{\beta_D \cos\theta} \Rightarrow \cos\theta = \frac{k\lambda}{D}\left(\frac{1}{\beta_D}\right) \tag{2}$$

3.2.2.2 Williamson–Hall methods Crystal imperfections and distortion of strain-induced peak broadening are related by $\varepsilon \approx \beta_S/\tan\theta$. There is an extraordinary property of Eq. (2) which has the dependency on the diffraction angle θ. Scherrer equation follows a $1/\cos\theta$ dependency but not $\tan\theta$ as W–H method. It is well known that both microstructural causes small crystallite size and microstrain occur together from the reflection broadening. Depending on different θ positions, the separation of size and strain broadening analysis is done using Williamson and Hall. The following results are the addition of the Scherrer equation and $\varepsilon \approx \beta_S/\tan\theta$.

$$\beta_{hkl} = \beta_S + \beta_D \tag{3}$$

$$\beta_{hkl} = \left(\frac{k\lambda}{D\cos\theta}\right) + 4\varepsilon\tan\theta \tag{4}$$

Rearranging Eq. (4) gives:

$$\beta_{hkl}\cos\theta = \left(\frac{k\lambda}{D}\right) + 4\varepsilon\sin\theta \tag{5}$$

Here, Eq. (5) is used for uniform deformation model (UDM) where the strain is assumed uniform in all crystallographic directions. $\beta\cos\theta$ was plotted with respect to

$4\sin\theta$ for the peaks of $Zn_{1-x}Mg_xO$ composites. Strain and particle size are calculated from the slope and y-intercept of the fitted line, respectively. From the lattice parameter calculations, it was observed that this strain might be due to the lattice shrinkage. The UDM analysis results are shown in Fig. 3. Then, we have calculated the values of stress $\sigma = Y\varepsilon$ and the energy density $u = (\varepsilon^2 Y_{hkl})/2$ using the Hooke's law, where ε is the strain and Y is the Young's modulus.

For a hexagonal crystal, Young's modulus is given by the following relation [25]:

$$Y_{hkl} = \left(\frac{\left(h^2 + \frac{(h+2k)^2}{3} + \left(\frac{al}{c}\right)^2\right)^2}{S_{11}\left(h^2 + \frac{(h+2k)^2}{3}\right)^2 + S_{33}\left(\frac{al}{c}\right)^4 + (2S_{13}+S_{44})\left(h^2 + \frac{(h+2k)^2}{3}\left(\frac{al}{c}\right)^2\right)} \right) \quad (6)$$

where S_{11}, S_{13}, S_{33} and S_{44} are the elastic compliances of ZnO with values of 7.858×10^{-12}, -2.206×10^{-12}, 6.940×10^{-12} and 23.57×10^{-12} $m^2\ N^{-1}$, respectively [26]. Young's modulus, Y, for hexagonal $Zn_{1-x}Mg_xO$ composites was calculated as $\approx$127.5 GPa. The same value of Y has been found on nanoparticles of Ni-doped zinc oxide [27]. In added, Prabhu et al. [28] found a value of Young's modulus in the order of 130 GPa for Fe-doped ZnO nanoparticles. In Table 1, the results attained from Scherrer method and Williamson–Hall (W–H) analysis are summarized.

Table 1 shows that the average crystallite size of the $Zn_{1-x}Mg_xO$ composites decreases with the increase in the Mg concentration from the different models, implying that the inclusion of strain in different forms has very little effect on the average crystallite size. It is found that the values of stress, strain and energy density increase with the increase in the doping rate.

3.3 Electrical properties

The impedance spectroscopy is an important tool to investigate the dielectric and electrical properties of polymers and ceramics in wide ranges of temperatures and frequencies. To characterize the AC conductivity in the samples under study, dielectric measurements have been taken in the frequency range (0.1–10^6 Hz) and temperature range (173–373 K). Figure 4 shows the dependence of the AC conductivity of ZnMgO composites on the frequency of the applied field at various temperatures. In the frequency range of 0.1–10 Hz, Fig. 4b shows linear increase in conductivity with the increase in the frequency and the temperature. This effect can be caused by the humidity of the cell at low temperatures (<0 °C), which introduces the water molecules in the pellet ZnMgO.

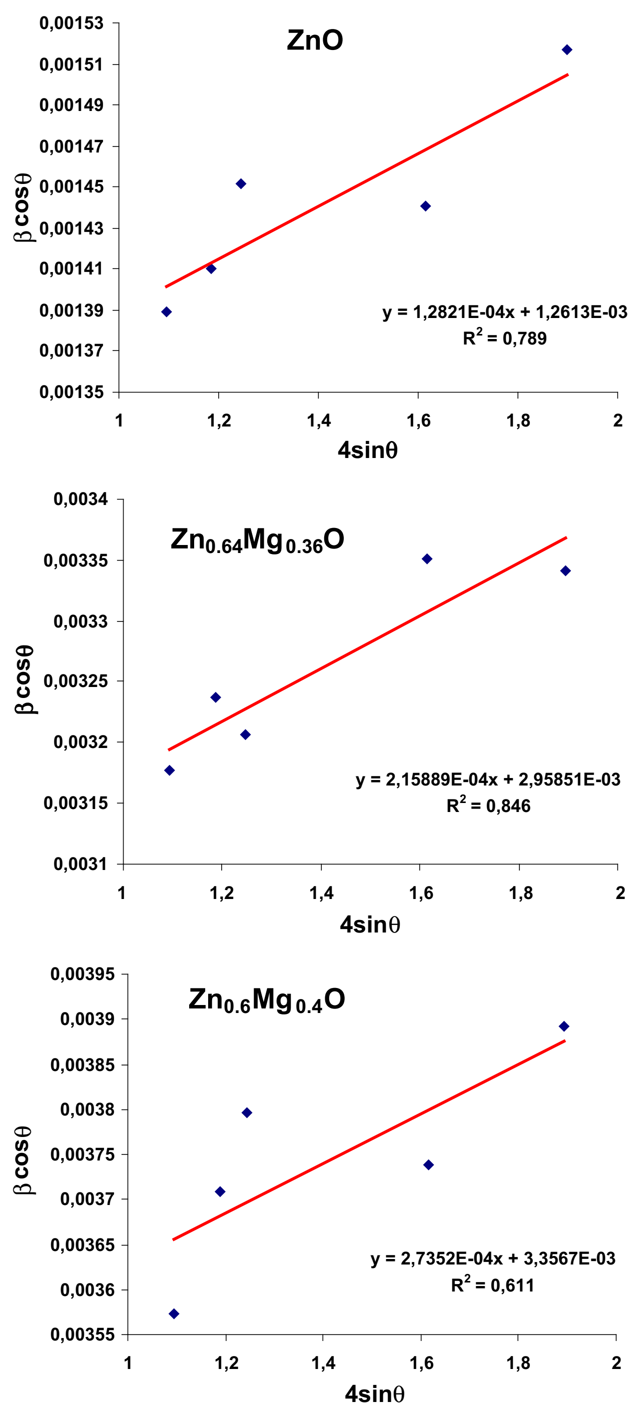

Fig. 3 W–H analysis of $Zn_{1-x}Mg_xO$ composites assuming UDM. Fit to the data, the strain is extracted from the slope and the crystalline size is extracted from the y-intercept of the fit

It is worthy to note that AC conductivity depended on both frequency and temperature and increased up. All the spectra exhibited the typical behavior of ionic disordered materials [29–34]. In the low-frequency region, the AC conductivity patterns showed a frequency-independent plateaux and exhibited dispersion at higher frequencies.

Table 1 Geometric parameters of $Zn_{1-x}Mg_xO$ composites

Compound	Method				
	Scherrer	Williamson–Hall (W–H)			
$Zn_{1-x}Mg_xO$	D (nm)	D (nm)	ε unit $\times 10^{-4}$	$\sigma \times 10^{6}$	$u \times 10^{3}$
$x = 0$	109.74	114.81	1.28	16.31	1.04
$x = 36$	44.40	48.94	2.15	27.47	2.96
$x = 40$	38.73	43.14	2.73	34.80	4.75

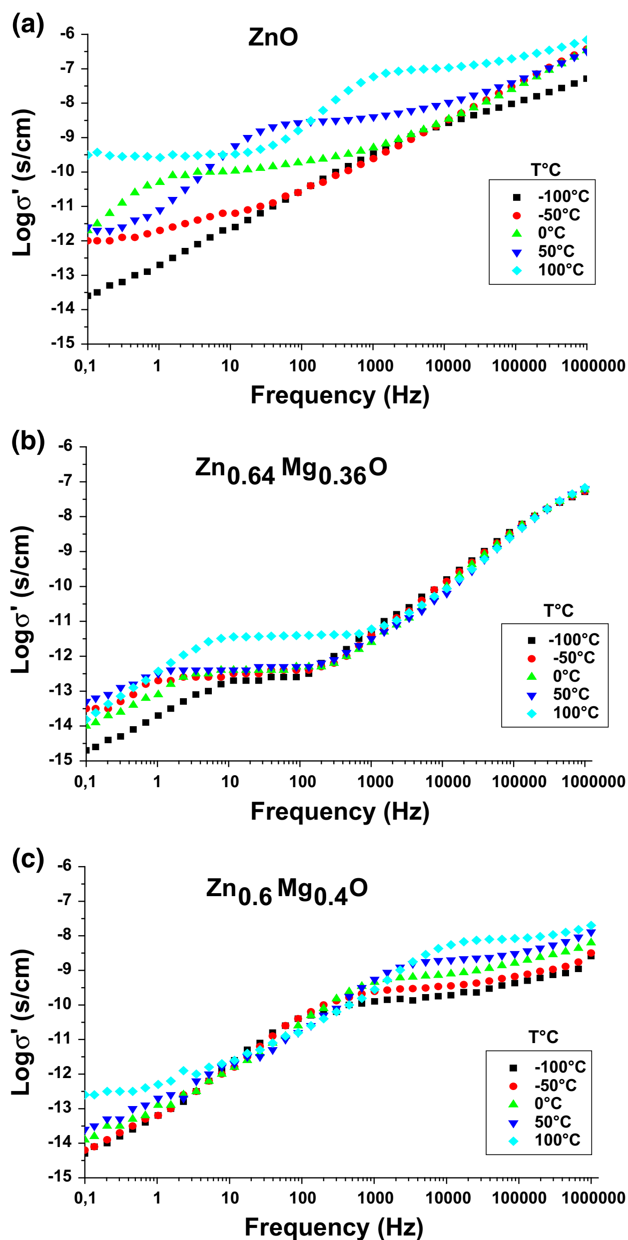

Fig. 4 Variation of the AC conductivities for ZnO (**a**), $Zn_{0.64}Mg_{0.36}O$ (**b**) and $Zn_{0.60}Mg_{0.40}O$ (**c**) as a function of frequency and at various temperatures

This behavior is generally related to the mechanism of charge transport as well as the many-body interaction among charge carriers [35].

At low frequencies (Fig. 4a–c), when the applied electric field forced the charge carriers to drift over large distances, as temperature was increased, a tendency to retain almost constant values was recorded. When the frequency was increased, after reaching the critical frequency ω_p, the mean displacement of the charge carriers was reduced with the real part of the conductivity following the law σ_{ac} (ω, T) $\approx \omega^s$ with $0 \le s \le 1$, characterizing the hopping conduction [36, 37]. The hopping process means a sudden displacement of a charge carrier from one position to another and includes both jumps over a potential barrier and quantum mechanical tunneling [38, 39].

The frequency–temperature dependence of the AC conductivity is well described by the Jonsher's equation [40]:

$$\sigma_{ac}(\omega, T) = \sigma_{dc}(T) + A(T)\omega^s \quad (7)$$

where $\sigma_{dc}(T)$ is the $\omega \to 0$ limit value of σ_{ac} (ω, T) and corresponds to the DC conductivity values. A and s are parameters depending on the temperature [41]. The parameter s describes the slope of the power law behavior and usually varies between 0 and 1.

Gradually, it is noted that the plateau of the conductivity broadens with frequency when the temperature varies from −100 to 100 °C, with the increase in Mg concentration.

It is shown that the DC conductivities of the doped ZnO samples decrease logarithmically with the increase in Mg doping rate. This decrease might be caused by sintering and ions diffusion processes [42]. Another reason for this decrease might be the high Mg doping composition which can introduce deep donor levels between valance and conduction bands. Actually, the Mg doping in the ZnO may produce electrical barriers, increasing the scattering of the carriers, and thus decreasing the conductivity [4, 9, 50]. Similarly, Li et al. [43] have observed an increase in the resistivity from 0.19 to 1.5×10^2 (Ω cm) and a decrease in the mobility from 14.3 to 6.8 ($cm^2\ V^{-1}\ s^{-1}$) of the Mg-doped ZnO with increasing Mg concentration from 0.02 to 0.22, respectively. In our case, the

band gap is increased from 3.28 eV for undoped ZnO to 3.822 eV for $Zn_{0.6}Mg_{0.4}O$ film [16]. Hence, such augmentation in the band gap could be caused by the logarithmic decrease in the conductivity with increasing Mg concentration.

3.3.1 Direct current conductivity

The DC conductivity, originating from the charge carriers, increases with the increase in temperature and obeys to the Arrhenius law:

$$\sigma_{dc} = \sigma_0 \exp\left(\frac{-E_A}{kT}\right) \quad (8)$$

where σ_0 is the conductivity at infinite temperature, E_A is the activation energy, k is the Boltzmann's constant and T is the temperature in Kelvin. The dependence of logarithmic DC conductivity, ln σ_{dc}, on the inverse of temperature, 1000/T, for ZnMgO composites is shown in Fig. 5.

From the linear slopes of the curves ln$\sigma_{dc} = f(1000/T)$, the activation energies of our ZnMgO composites are determined and given in Table 2.

For the ZnO sample, one value of activation energy of about 0.38 eV was found. Similar values have been reported in previous research works [44–47] which are attributed to oxygen vacancy impurities V_O.

Two different activation energies (E_{A1} and E_{A2}) are obtained for the doped samples ZnMgO. The first value 0.09 eV is very near to 0.1 eV, which is associated with an oxygen interstitials O_i^+ and O_i^0 [48, 49]. As for the second values 0.72 and 0.8 eV, they are associated with the MWS polarization [50, 51].

3.3.2 Alternating current conductivity

Concerning the frequency dependency on conductivity, the data imply a power law given by:

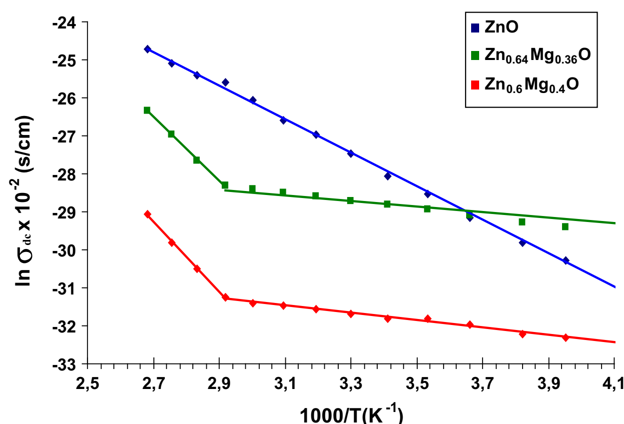

Fig. 5 Variation of logarithmic conductivity, ln σ_{dc}, with inverse temperature, 1000/T, for ZnO pure, $Zn_{0.64}Mg_{0.36}O$ and $Zn_{0.60}Mg_{0.40}O$

Table 2 Activation energies of $Zn_{1-x}Mg_xO$ composites

Mg content	E_{A1} (eV)	E_{A2} (eV)
0	0.38	
0.36	0.09	0.72
0.40	0.09	0.80

$$\sigma_{ac} = \sigma_{ac}(\omega, T) = A(T)\omega^s \quad (9)$$

where ω is the angular frequency and A and s are the temperature-dependent parameters. To determine the predominant conduction mechanism of the AC conductivity of the sample, the appropriate model can be suggested for the conduction mechanism in the light of the different theoretical models correlating the conduction mechanism of AC conductivity with $s(T)$ plots (Fig. 6). In the literature, various models have been proposed to explain the behavior of the exponent s such as the quantum mechanical tunneling (QMT) model, the small polaron tunneling (SPT) model, the correlated barrier hopping (CBH) model and the overlapping large polaron tunneling (OLPT) model.

(i) According to the QMT model, the exponent s is almost equal to 0.8 and slightly increases with temperature or independent of temperature [52].
(ii) According to SPT model [53, 54], the exponent s increases with the increase in temperature.
(iii) In the OLPT model, the exponent s depends on both frequency and temperature and drops to a minimum value, and then increases with the rise in temperature [55].
(iv) In the CBH model, the charge carrier hops between sites over the potential barrier separating them and the frequency exponent s is ranged from 0.7 to 1 at room temperature and is found to decrease with the increase in temperature [56, 57].

For the ZnO sample, it is found that the exponent s decreases from 1.07 to 0.50 with the increase in temperature. This behavior is in accordance with the CBH model [56, 57].

Concerning the sample $Zn_{0.64}Mg_{0.36}O$, there are two conduction mechanisms which depend on the frequency:

- For the first frequency region (600 Hz–17 kHz), the value of s varies from 0.7 to 1 and decrease with the increase in temperature. This is in good agreement with the CBH model [56, 57].
- For the second frequency region (17 kHz–1 MHz), the value of s increases from 0.86 to 1.06 as a function of temperature. This behavior is in accordance with the SPT model [53, 54].

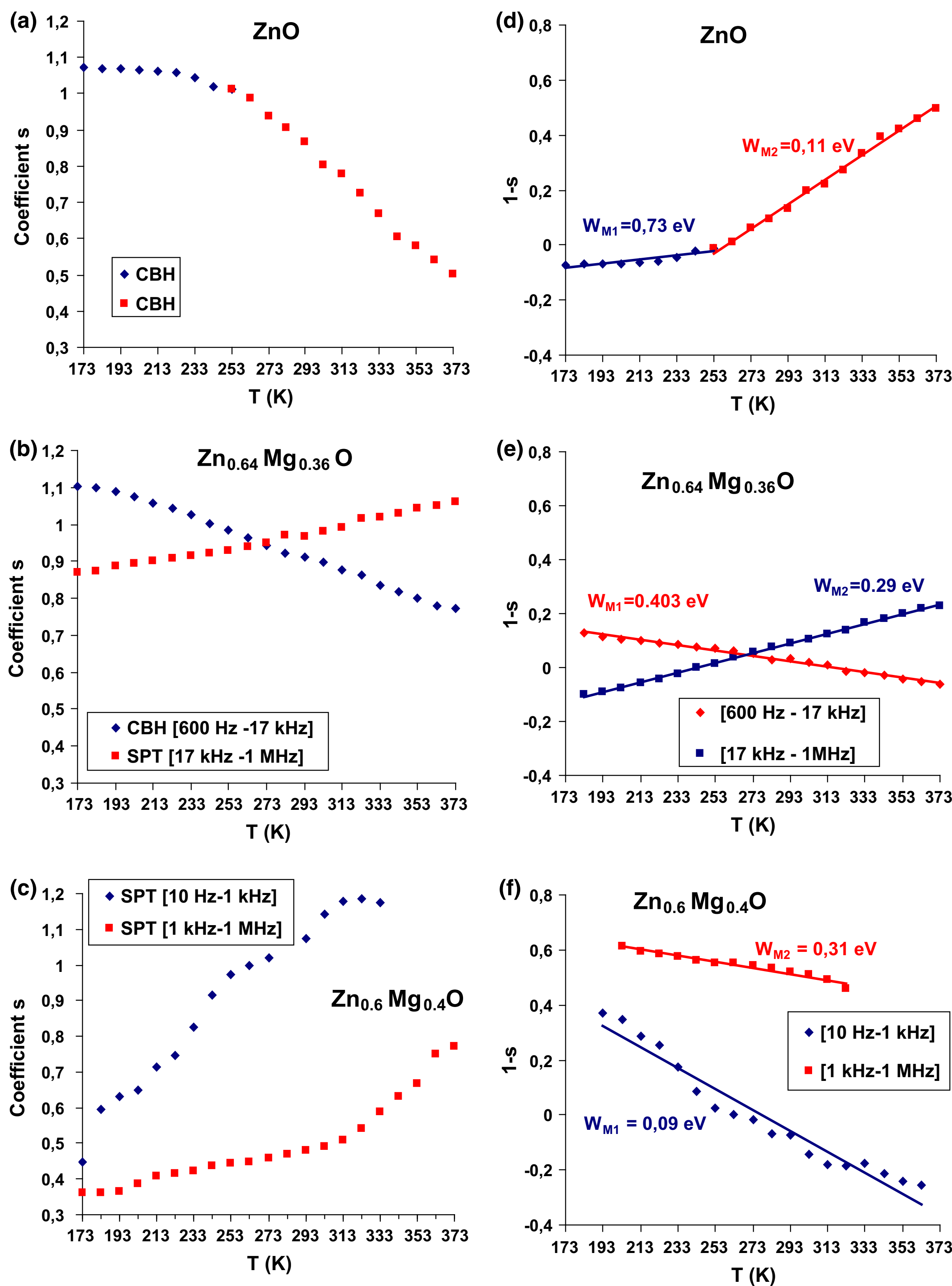

Fig. 6 Variation of the exponent s and parameter $(1 - s)$ with the temperature

But for the $Zn_{0.60}Mg_{0.40}O$ composites, the same conduction mechanisms are found in the two frequency ranges:

- For the first frequency region (10 Hz–1 kHz), it is found that the value of s increases from 0.63 to 1.25 with the increase in temperature when it varies from

−100 to 100 °C, respectively. This behavior is in harmony with the SPT model [53, 54].

- For the second frequency region (1 kHz → 1 MHz), the values of s increases as a function of temperature from 0.32 to 0.77. This is in good agreement with the SPT model [53, 54].

3.3.2.1 Correlated barrier hopping (CBH) model In the CBH conduction model, the exponent s is found to obey the following equation [58]:

$$s = 1 - \frac{6k_B T}{W_M} \tag{10}$$

where W_M is the maximum barrier height at infinite separation, which is called the "polaron binding energy," i.e., the binding energy of the carrier in its localized sites. For the neighboring sites at a separation R_ω, the Coulomb wells overlap, resulting in a lowering of the effective barrier from W_M to the value W_m. For the case of a single-electron transition, this is given by:

$$W_m = W_M - \frac{e^2}{\pi \varepsilon' \varepsilon_0 R_\omega} \tag{11}$$

where the hopping distance (R_ω) at frequency ω and temperature T is given by:

$$R_\omega = \frac{e^2}{\pi \varepsilon' \varepsilon_0 (W_M - k_B T \ln(1/\omega \tau_0))} \tag{12}$$

where τ_0 is a characteristic relaxation time which is of the order of an atomic vibration period, k_B is the Boltzmann constant, ε' is the real part of dielectric constant and ε_0 is the dielectric permittivity of vacuum. Thus, the lower bound (cutoff) to hopping distance becomes:

$$R_{min} = \frac{e^2}{\pi \varepsilon' \varepsilon_0 W_M} \tag{13}$$

The $(1 - s)$ values were plotted versus temperature T, and its slope is used to calculate the binding energy W_M (Fig. 6d, e). The hopping distance R_ω, the lower bound (cutoff) R_{min} and the Columbic barrier height W_m are calculated using Eqs. (5–7), respectively. The values of AC parameters, R_{min} and W_m at different frequencies are listed in Table 3 at 173 K.

The density of states at the Fermi level can be estimated from the following expression [59]:

$$N(E_F) = \frac{3}{4\pi R_\omega^3 W_M} \tag{14}$$

It is clear that the values of W_m and R_ω decrease with the increase in frequency, which may explain the increase in AC electrical conductivity for higher frequencies.

The obtained values of $N(E_F)$ that are reported in Table 3 are in the range of 9.27×10^{17}–1.90×10^{20} eV^{-1} cm^{-3}. The density of states at Fermi level decreased with the increase in MgO.

Finally, we can conclude that the Mg doping is a promising way to improve the electrical properties of ZnO-based devices.

3.3.2.2 The small polaron tunneling (SPT) model According to the small polaron model (SPT), the AC conductivity $\sigma(\omega)$ and the exponent s are given by,

$$\sigma(\omega) = \pi^2 e^2 kT \alpha^{-1} [N(E_F)]^2 \frac{\omega R_\omega^4}{12} \tag{15}$$

and

$$s = 1 - \frac{4}{[\ln(1/\omega\tau_0) - W_H/kT]} \tag{16}$$

For the large values of $W_H/k_B T$, the exponent s becomes:

Table 3 Physical properties and polaron hopping parameters of $Zn_{1-x}Mg_xO$ composites

Mg content	W_M (eV)	Frequency (Hz)	R_ω (nm)	R_{min} (nm)	W_m (eV)	$N(E_F)$ eV^{-1} cm^{-3}
0	0.748	87792	3.389	2.403	0.214	$8.30 \times 10^{+18}$
		197530	3.392	2.460	0.202	$8.28 \times 10^{+18}$
		444440	3.378	2.506	0.190	$8.39 \times 10^{+18}$
		1000000	3.350	2.540	0.178	$8.59 \times 10^{+18}$
	0.114	87792	7.041	1.545	0.1371	$5.95 \times 10^{+18}$
		197530	7.200	1.582	0.1375	$5.57 \times 10^{+18}$
		444440	7.324	1.611	0.1378	$5.29 \times 10^{+18}$
		1000000	7.418	1.633	0.1380	$5.09 \times 10^{+18}$
0.36	0.290	676.64	53.669	0.4871	0.287	$5.32 \times 10^{+18}$
		1015	16.290	0.4875	0.281	$1.90 \times 10^{+18}$
		1522	9.611	0.4878	0.275	$9.27 \times 10^{+18}$
		2283	6.818	0.4881	0.269	$2.59 \times 10^{+18}$

Table 4 AC conductivity parameters of $Zn_{0.64}Mg_{0.36}O$ and $Zn_{0.60}Mg_{0.40}O$ composites at $T = 373$ K and different frequencies

Mg content	W_M (eV)	Frequency (Hz)	σ_{ac} (S cm^{-1})	R_ω (nm)	$N(E_F)$ eV^{-1} cm^{-3}
0.36	0.402	7707.3	5.19×10^{-11}	6.639	$2.029 \times 10^{+18}$
		58528	1.24×10^{-9}	4.611	$6.054 \times 10^{+18}$
		296300	1.66×10^{-8}	2.989	$2.222 \times 10^{+19}$
		1000000	6.75×10^{-8}	1.773	$1.064 \times 10^{+20}$
0.40	0.09	7707.3	4.25×10^{-9}	0.163	$6.073 \times 10^{+17}$
		58528	7.97×10^{-9}	0.143	$9.036 \times 10^{+17}$
		296300	1.07×10^{-8}	0.126	$1.296 \times 10^{+18}$
		1000000	1.98×10^{-8}	0.114	$1.753 \times 10^{+18}$
	0.31	7707.3	4.25×10^{-9}	9.407	$9.159 \times 10^{+17}$
		58528	7.97×10^{-9}	7.380	$1.897 \times 10^{+18}$
		296300	1.07×10^{-8}	5.758	$3.993 \times 10^{+18}$
		1000000	1.98×10^{-8}	4.542	$8.138 \times 10^{+18}$

$$s = 1 - \frac{4k_B T}{W_H} \quad (17)$$

where the tunneling distance $R\omega$ at frequency ω is given by:

$$R_\omega = \frac{1}{2\alpha}\left[\ln\left(\frac{1}{\omega\tau_0}\right) - \frac{W_H}{kT}\right] \quad (18)$$

In the above equations, α^{-1} is the spatial extension of the polaron, R_ω the tunneling distance, τ_0 the characteristic relaxation time, W_H the polaron hopping energy and $N(E_F)$ the density of states near Fermi level. According to the literature, the average value of the spatial extension α is 5×10^6 cm^{-1} [60, 61]. The experimental values of s at different temperatures and frequencies were fitted to Eq. (11) taking W_H as a parameter (Fig. 6e, f). Our results are in good agreement with the results found by Kılınç et al. [11]. The value of τ_0 was taken as 10^{-13} s [62]. Table 4 summarizes the values of the extracted parameters.

The obtained values of N are reasonable for localized states [61] where the tunneling distances R_ω are in the nanoscale range of 0.1 to 10 nm. Besides, the values of W_M decrease with the increase in the MgO content. This result is readily explained by the decrease in the conductivity. The CBH conduction mechanism appears for undoped ZnO. However, the conductivity mechanisms OLPT and SPT are dominant for Mg-doped ZnO films. This distinction of conduction models is sensitively dependent on the Mg doping concentration.

4 Conclusion

The effect of Mg doping on morphological, structural and electrical properties of ZnO ceramics has been investigated. In fact, the grain size and density of the crystallites are reduced with the increase in the Mg doping concentration. The X-ray diffraction reveals that all the samples are polycrystalline and have a prominent hexagonal crystalline structure with (002) and (101) as preferred growth directions. The formation of the hexagonal ZnMgO alloy phase and the segregation of MgO-cubic phase took place for higher concentrations. The crystallite size, strain and stress were studied using Williamson–Hall (W–H) method. The results of mean particle size of $Zn_{1-x}Mg_xO$ composites showed an inter-correlation with W–H analysis and Sherrer method. Besides, the electrical measurements were taken to identify the conductivity mechanisms in these samples. Results have shown the presence of electron traps with activation energies between 0.09 and 0.8 eV. Furthermore, the AC conductivity is found to decrease logarithmically with the increase in Mg doping. From temperature dependence analyses, it has been shown that the AC conductivity is controlled by the hopping correlated barrier (CBH) model for the ZnO sample and the small polaron tunneling (SPT) model for $Zn_{0.64}Mg_{0.36}O$ and $Zn_{0.60}Mg_{0.40}O$ composites.

References

1. B.B. Rao, Mater. Chem. Phys. **64**, 62 (2000)
2. R.W. Birkmire, E. Eser, Annu. Rev. Mater. Sci. **27**, 625 (1997)
3. T. Aoki, Y. Hatanaka, D.C. Look, Appl. Phys. Lett. **76**, 3257 (2000)
4. Mariem Chaari, Adel Matoussi, Phys. B **407**, 3441 (2012)
5. Y.R. Ryu, T.S. Lee, Appl. Phys. Lett. **83**, 87 (2003)
6. T.V. Vimalkumar, N. Poornima, C. Sudha Kartha, K.P. Vijayakumar, Mater. Sci. Eng. B **175**, 29 (2010)
7. A. Tiburcio-Silver, J.C. Joubert, M. Labeau, J. Phys. III Fr. **2**, 1287 (1992)
8. M.M. Hassan, S.A. Ahmed, M. Chaman, W. Khan, A.H. Naqvi, A. Azam, Mater. Res. Bull. **47**, 3952 (2012)
9. M. Chaari, A. Matoussi, Mater. Sci. Eng. B **178**, 1130 (2013)
10. F. Ahmed, S. Kumar, N. Arshi, M.S. Anwar, S.N. Heo, B.H. Koo, Acta Mater. **60**, 5190 (2012)

11. N. Kılınç, L. Arda, S. Öztürk, Z.Z. Öztürk, Cryst. Res. Technol. **45**(5), 29 (2010)
12. G.H. Ning, X.P. Zhao, J. Li, Opt. Mater. **27**, 1 (2004)
13. Z.Q. Ma, W.G. Zhao, Y. Wang, Thin Solid Films **515**, 8611 (2007)
14. D.X. Zhao, Y.C. Liu, D.Z. Shen, Y.M. Lu, J.Y. Zhang, X.W. Fan, J. Cryst. Growth **234**, 427 (2002)
15. J.S. Park, Y.H. Han, J. Eur. Ceram. Soc. **27**, 1077 (2007)
16. Z.J. Othman, A. Matoussi, F. Fabbari, F. Rossi, G. Salviati, J. Appl. Phys. A **116**(3), 1501 (2014)
17. H. Yoon, G. Nam, H. Park, J.-S. Son, J.-Y. Leem, Electron. Mater. Lett. **9**(4), 545 (2013)
18. A. Shukla, V.K. Kaushik, D. Prasher, Electron. Mater. Lett. **10**(1), 61 (2014)
19. S.M. Park, G.H. Gu, C.G. Park, Phys. Status Solidi A **208**(11), 2688 (2011)
20. P.K. Kannan, R. Saraswathi, J.B.B. Rayappan, Sens. Actuators A Phys. **164**, 8 (2010)
21. Q. Zheng, F. Huang, K. Ding, J. Huang, D. Chen, Z. Zhan, Z. Lin, Appl. Phys. Lett. **98**, 221112 (2011)
22. P. Cao, Y. Bai, D.X. Zhao, D.Z. Shen, Mater. Sci. Semicond. Process. **14**, 73 (2011)
23. R. Yogamalar, R. Srinivasan, A. Vinu, K. Ariga, A.C. Bose, Solid State Commun. **149**, 1919 (2009)
24. K.D. Rogers, P. Daniels, Biomaterials **23**, 2577 (2002)
25. J.-M. Zhang, Y. Zhang, K.-W. Xu, V. Ji, Solid State Commun. **139**, 87 (2006)
26. J.F. Nye, *Physical Properties of Crystals: Their Representation by Tensors and Matrices* (Oxford University Press, Oxford, 1985)
27. S. Thakur, J. Kumar, J. Sharma, N. Sharma, P. Kumar, J. Optoelectron. Adv. Mater. **15**(7–8), 989 (2013)
28. Y.T. Prabhu, K. Venkateswara Rao, V. Sesha Sai Kumar, B. Siva Kumari, Int. J. Eng. Adv. Technol. **2**(4), 2249 (2013)
29. D.L. Sidebottom, Phys. Rev. Lett. **83**, 983 (1999)
30. B. Roling, A. Happe, K. Funke, M.D. Ingram, Phys. Rev. Lett. **78**, 2160 (1997)
31. S. Capaccioli, M. Lucchesi, P.A. Rolla, G. Ruggeri, J. Phys, Condens. Matter **10**, 5595 (1998)
32. D.S. Mc Lachlan, M.B. Heaney, Phys. Rev. B **60**, 12746 (1999)
33. M.T. Connor, S. Roy, T.A. Ezquerra, F.J. Balta Calleja, Phys. Rev. B **57**, 2286 (1998)
34. P. Pötschke, S.M. Dudkin, I. Alig, Polymer **44**, 5023 (2003)
35. F. Kremer, A. SchÖnhals, *Broadband Dielectric Spectroscopy* (Springer, Heidelberg, 2002)
36. J.C. Dyre, T.B. Schroeder, Rev. Mod. Phys. **72**, 873 (2000)
37. G.C. Psarras, E. Manolakaki, G.M. Tsangaris, Compos. A **34**, 1187 (2003)
38. H. Böttger, U.V. Bryskin, *Hopping Conduction in Solids*, vol. 41 (Verlag Akademie, Berlin, 1985), p. 69
39. G.C. Psarras, Compos. A **37**, 1545 (2006)
40. A.K. Jonsher, Nature **267**, 673 (1977)
41. G.M. Tsangaris, G.C. Psarras, E. Manolakaki, Adv. Compos. Lett. **8**, 25 (1999)
42. J.P. Han, P.Q. Mantas, A.M.R. Senos, J. Eur. Ceram. Soc. **21**, 1183 (2001)
43. Y. Li, R. Deng, B. Yao, G. Xing, D. Wang, W. Tom, Appl. Phys. Lett. **97**, 102506 (2010)
44. J.F. Cordaro, Y. Shim, J.E. May, J. Appl. Phys. **60**, 4186 (1986)
45. A. Rohatgi, S.K. Pang, T.K. Gupta, W.D. Straub, J. Appl. Phys. **63**, 5375 (1988)
46. Y. Shim, J.F. Cordaro, J. Am. Ceram. Soc. **71**, 184 (1988)
47. G. Garcia-Belmonte, J. Bisquert, F. Fabregat-Santiago, Solid State Electron. **43**, 2123 (1999)
48. S. Li, P. Cheng, J. Li, L. Zhao, in *Proceedings of the IEEE International Conference on Solid Dielectric*, ICSD pp. 207–210 (2007)
49. A.F. Kohan, G. Ceder, D. Morgan, C.G. van de Walle, Phys. Rev. B **61**, 15019 (2000)
50. C.-W. Nahm, Ceram. Int. **36**, 1109 (2010)
51. K.C. Kao, *Dielectric Phenomena in Solids with Emphasis on Physical Concepts of Electronic Processes* (Elsevier Academic Press, San Diego, 2004), pp. 430–432
52. S.A. Mansour, I.S. Yahia, F. Yakuphanoglu, Dyes Pigment. **87**, 144 (2010)
53. N.F. Mott, J. Non-Cryst. Solids **1**, 1 (1968)
54. M.H. Buraidah, L.P. Teo, S.R. Majid, A.K. Arof, Phys. B **404**, 1373 (2009)
55. J.T. Gudmundsson, H.G. Svavarsson, S. Gudjonsson, H.P. Gislason, Phys. B **340**, 324 (2003)
56. T. Winie, A.K. Arof, Ionics **10**, 193 (2004)
57. W. Jung, Phys. B **403**, 636 (2008)
58. G.E. Pike, Phys. Rev. B **6**, 1572 (1972)
59. N.F. Mott, E.A. Davis, *Electronic Processes in Non-Crystalline Materials*, 2nd edn. (Clarendon Press, Oxford, 1979)
60. N. Kılınc, S. Ozturk, L. Arda, A. Altındal, Z.Z. Ozturk, J. Alloys Compd. **536**, 138 (2012)
61. H. Li, H. Qiu, Y. Mingpeng, X. Chen, Mater. Chem. Phys. **26**, 866 (2011)
62. A.R. Long, Adv. Phys. **31**, 553 (1982)